

1 The Silicon Vertex Detector of the Belle II Experiment

2 Y. Uematsu^r, K. Adamczyk^u, L. Aggarwal^l, H. Aihara^r, T. Aziz^k, S. Bacher^u,
3 S. Bahinipati^f, G. Batignani^{l,m}, J. Baudot^e, P. K. Behera^g, S. Bettarini^{l,m},
4 T. Bilka^c, A. Bozek^u, F. Buchsteiner^b, G. Casarosa^{l,m}, L. Corona^{l,m},
5 T. Czank^q, S. B. Das^h, G. Dujany^e, C. Finck^e, F. Forti^{l,m}, M. Friedl^b,
6 A. Gabrielli^{n,o}, E. Ganiev^{n,o}, B. Gobbo^o, S. Halder^k, K. Hara^{s,p}, S. Hazra^k,
7 T. Higuchi^q, C. Irmiler^b, A. Ishikawa^{s,p}, H. B. Jeon^t, Y. Jin^{n,o}, C. Joo^q,
8 M. Kaleta^u, A. B. Kaliyar^k, J. Kandra^c, K. H. Kang^q, P. Kapusta^u,
9 P. Kodyš^c, T. Kohriki^s, M. Kumar^h, R. Kumarⁱ, C. La Licata^q, K. Lalwani^h,
10 R. Leboucher^d, S. C. Lee^t, J. Libby^g, L. Martel^e, L. Massaccesi^{l,m},
11 S. N. Mayekar^k, G. B. Mohanty^k, T. Morii^q, K. R. Nakamura^{s,p},
12 Z. Natkaniec^u, Y. Onuki^r, W. Ostrowicz^u, A. Paladino^{l,m}, E. Paoloni^{l,m},
13 H. Park^t, L. Polat^d, K. K. Rao^k, I. Ripp-Baudot^e, G. Rizzo^{l,m}, D. Sahoo^k,
14 C. Schwanda^b, J. Serrano^d, J. Suzuki^s, S. Tanaka^{s,p}, H. Tanigawa^r,
15 R. Thalmeier^b, R. Tiwari^k, T. Tsuboyama^{s,p}, O. Verbycka^u, L. Vitale^{n,o},
16 K. Wan^r, Z. Wang^r, J. Webb^a, J. Wiechczynski^m, H. Yin^b, L. Zani^d,

17 (Belle-II SVD Collaboration)

18 ^a*School of Physics, University of Melbourne, Melbourne, Victoria 3010, Australia*

19 ^b*Institute of High Energy Physics, Austrian Academy of Sciences, 1050 Vienna, Austria*

20 ^c*Faculty of Mathematics and Physics, Charles University, 121 16 Prague, Czech Republic*

21 ^d*Aix Marseille Université, CNRS/IN2P3, CPPM, 13288 Marseille, France*

22 ^e*IPHC, UMR 7178, Université de Strasbourg, CNRS, 67037 Strasbourg, France*

23 ^f*Indian Institute of Technology Bhubaneswar, Satya Nagar, India*

24 ^g*Indian Institute of Technology Madras, Chennai 600036, India*

25 ^h*Malaviya National Institute of Technology Jaipur, Jaipur 302017, India*

26 ⁱ*Punjab Agricultural University, Ludhiana 141004, India*

27 ^j*Punjab University, Chandigarh 160014, India*

28 ^k*Tata Institute of Fundamental Research, Mumbai 400005, India*

29 ^l*Dipartimento di Fisica, Università di Pisa, I-56127 Pisa, Italy*

30 ^m*INFN Sezione di Pisa, I-56127 Pisa, Italy*

31 ⁿ*Dipartimento di Fisica, Università di Trieste, I-34127 Trieste, Italy*

32 ^o*INFN Sezione di Trieste, I-34127 Trieste, Italy*

33 ^p*The Graduate University for Advanced Studies (SOKENDAI), Hayama 240-0193, Japan*

34 ^q*Kavli Institute for the Physics and Mathematics of the Universe (WPI), University of*

35 *Tokyo, Kashiwa 277-8583, Japan*

36 ^r*Department of Physics, University of Tokyo, Tokyo 113-0033, Japan*

37 ^s*High Energy Accelerator Research Organization (KEK), Tsukuba 305-0801, Japan*

38 ^t*Department of Physics, Kyungpook National University, Daegu 41566, Korea*

39 ^u*H. Niewodniczanski Institute of Nuclear Physics, Krakow 31-342, Poland*

40 Abstract

41 The Silicon Vertex Detector (SVD) is a part of the vertex detector in the
42 Belle II experiment at the SuperKEKB collider (KEK, Japan). Since the start

43 of data taking in spring 2019, the SVD has been operating stably and reliably
44 with a high signal-to-noise ratio and hit efficiency, achieving good spatial resolu-
45 tion and high track reconstruction efficiency. The hit occupancy, which mostly
46 comes from the beam-related background, is currently about 0.5% in the in-
47 nermost layer, causing no impact on the SVD performance. In anticipation of
48 the operation at higher luminosity in the next years, two strategies to sustain
49 the tracking performance in future high beam background conditions have been
50 developed and tested on data. One is to reduce the number of signal waveform
51 samples to decrease dead time, data size, and occupancy. The other is to utilize
52 the good hit-time resolution to reject the beam background hits. We also mea-
53 sured the radiation effects on the sensor current, strip noise, and full depletion
54 voltage caused during the first two and a half years of operation. The results
55 show no detrimental effect on the SVD performance.

56 *Keywords:* Silicon strip detector, Vertex detector, Tracking detector, Belle II

57 1. Introduction

58 The Belle II experiment [1] aims to probe new physics beyond the Standard
59 Model in high-luminosity e^+e^- collisions at the SuperKEKB collider (KEK,
60 Japan) [2]. The main collision energy in the center-of-mass system is 10.58 GeV
61 on the $\Upsilon(4S)$ resonance, which enables various physics programs based on the
62 large samples of B mesons, τ leptons, and D mesons. Also, the asymmetric
63 energy of the 7 GeV electron beam and 4 GeV positron beam is adopted for
64 time-dependent CP violation measurements. The target of SuperKEKB is to
65 accumulate an integrated luminosity of 50 ab^{-1} with peak luminosity of about
66 $6 \times 10^{35} \text{ cm}^{-2}\text{s}^{-1}$. In June 2021, SuperKEKB recorded the world's highest
67 instantaneous luminosity of $3.1 \times 10^{34} \text{ cm}^{-2}\text{s}^{-1}$. The data accumulated before
68 July 2021 corresponds to an integrated luminosity of 213 fb^{-1} .

69 The Vertex Detector (VXD) is the innermost detector in the Belle II detector
70 system. The VXD has six layers: the inner two layers (layers 1 and 2) are the
71 Pixel Detector (PXD), and the outer four layers (layers 3 to 6) are the Silicon

72 Vertex Detector (SVD). The schematic cross-sectional view of the VXD is shown
 73 in Fig. 1. The PXD consists of DEPFET pixel sensors, and its innermost radius
 74 is 1.4 cm from the beam interaction point (IP). A detailed description of the
 75 SVD appears in Sec. 2.

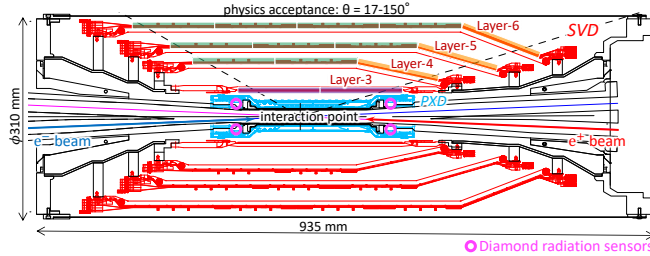


Figure 1: Schematic cross-sectional view of the VXD. The SVD is red, the PXD is light blue, and the IP beam pipe diamonds are pink circles. In the upper half of the VXD the locations of the three types of SVD DSSDs are indicated by boxes in three colors: purple for small sensors, green for large sensors, and orange for trapezoidal sensors as described in Tab. 1.

76 Diamond sensors [3], used to monitor the radiation dose and for the beam
 77 abort system, are mounted on the IP beam pipe and the bellows pipes outside of
 78 the VXD. The pink circles in Fig. 1 indicate the locations of the diamond sensors
 79 on the IP beam pipe. The diamond's measured doses are used to estimate
 80 the dose in the SVD. The diamond system also sends beam abort requests to
 81 SuperKEKB if the radiation level gets too high to avoid severe damage to the
 82 detector.

83 2. Belle II Silicon Vertex Detector

84 The SVD is crucial for extrapolating the tracks to the PXD to measure the
 85 decay vertices with the PXD and point at a region-of-interest limiting the PXD
 86 readout data volume. Other roles of the SVD are the standalone track recon-
 87 struction of low-momentum charged particles and their particle identification
 88 using ionization energy deposits. The SVD also plays a critical role in the decay
 89 vertex measurement of long-lived particles like K_S mesons, which decay inside
 90 the SVD volume.

91 The SVD [4] consists of four layers of double-sided silicon strip detectors
 92 (DSSDs). The material budget of the SVD is about 0.7% of a radiation length
 93 per layer. On each DSSD plane, a local coordinate is defined with u and v :
 94 u -axis along n-side strips and v -axis perpendicular to u -axis. In other words,
 95 p-side strips and n-side strips provide u and v information, respectively. In the
 96 cylindrical coordinate, u corresponds to r - φ information and v corresponds to
 97 z information. The SVD consists of three types of sensors: “small” rectangular
 98 sensors in layer 3, “large” rectangular sensors in the barrel region of layers 4, 5,
 99 and 6, and “trapezoidal” sensors in the forward region of layers 4, 5, and 6, which
 100 is slanted. They are indicated by purple, green, and orange boxes in Fig. 1. The
 101 main characteristics of these three types of sensors are summarized in Tab. 1.
 102 The sensors are manufactured by two companies: the small and large sensors
 103 by Hamamatsu and trapezoidal sensors by Micron. The full depletion voltage is
 104 60 V for Hamamatsu sensors and 20 V for Micron sensors; both types of sensors
 105 are operated at 100 V. In total, 172 sensors are assembled, corresponding to a
 106 sensor area of 1.2 m² and approximately 224,000 readout strips.

	Small	Large	Trapezoidal
No. of u/p-strips	768	768	768
u/p-strip pitch	50 μm	75 μm	50–75 μm
No. of v/n-strips	768	512	512
v/n-strip pitch	160 μm	240 μm	240 μm
Thickness	320 μm	320 μm	300 μm
Manufacturer	Hamamatsu		Micron

Table 1: Table of the main characteristics of the three types of sensors. Only readout strips are taken into account for number of strips and strip pitch. All sensors have one intermediate floating strip between two readout strips.

107 Sensor strips are AC coupled to the front-end ASIC, the APV25 [5], which
 108 was originally developed for the CMS Silicon Tracker. The APV25 tolerates
 109 more than 100 Mrad of radiation. It has 128 channels with a shaping time of
 110 about 50 ns. For the SVD, the APV25 is operated in “multi-peak” mode. The

111 mechanism of the data sampling in the multi-peak mode is explained in Fig. 2.
112 The chip samples the height of the signal waveform with the 32 MHz clock (31 ns
113 period) and stores each sample's information in an analog ring buffer. Since
114 the bunch-crossing frequency is eight times faster than the sampling clock, the
115 stored samples are not synchronous to the beam collision, in contrast to CMS,
116 which motivates operation in the multi-peak mode. In the present readout
117 configuration (the six-samples mode), at every reception of the Belle II global
118 Level-1 trigger, the chip reads out six successive samples of the signal waveform
119 stored in the buffers. The six-samples mode offers a wide enough time window
120 ($6 \times 31 \text{ ns} = 187 \text{ ns}$) to accommodate large timing shifts of the trigger. In
121 preparation for operation with higher luminosity, where background occupancy,
122 trigger dead-time, and the data size increase, we developed the three/six-mixed
123 acquisition mode (mixed-mode). The mixed-mode is a new method to read
124 out the signal samples from the APV25, in which the number of the samples
125 changes between three and six in each event, depending on the timing precision
126 of each Level-1 trigger signal in that event. For triggers with precise timing,
127 three-samples data are read out and the data have half time window and half
128 data size compared to ones of six-samples data, resulting in the reduction of the
129 effects due to higher luminosity. This functionality was already implemented
130 in the running system and confirmed by a few hours of smooth physics data
131 taking. Before we start to use the mixed-mode, the effect on the performance
132 due to the change of the acquisition mode is to be assessed. As the first step,
133 the effect in the hit efficiency was evaluated as described in Sec. 3.

134 The APV25 chips are mounted on each middle sensor (chip-on-sensor con-
135 cept) with thermal isolation foam in between. The merit of this concept is
136 shorter signal propagation length, leading to smaller capacitance of the signal
137 line and hence reduced noise level. To minimize the material budget the APV25
138 chips on the sensor are thinned down to 100 μm . The APV25 chips are mounted
139 on a single side of the sensor and readout of the signals from the opposite side is
140 performed via wrapped flexible printed circuits. The power consumption of the
141 APV25 chip is 0.4 W/chip and 700 W in the entire SVD. The chips are cooled

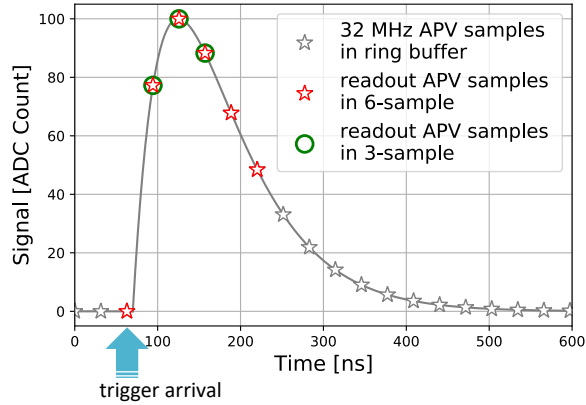


Figure 2: Example of sampling in “multi-peak” mode of the APV25. The gray line shows the signal waveform after the CR-RC shaper circuit. The stars show the sampled signal height recorded in the analog ring buffer according to the 32 MHz sampling clock. The red stars indicate the six successive samples read out at the trigger reception in the six-samples mode. The red stars with a green circle indicate the samples read out in the three-samples acquisition.

142 by a bi-phase -20°C CO_2 evaporative cooling system.

143 3. Performance

144 Since March 2019, the SVD has been operating reliably and smoothly for
 145 two and a half years. The total fraction of masked strips is about 1%. There
 146 was only one issue where one APV25 chip (out of 1,748 chips) was disabled
 147 during the spring of 2019, which was remediated by reconnecting a cable in the
 148 summer of 2019.

149 The SVD has also demonstrated stable and excellent performance [6]. The
 150 hit efficiency is continuously over 99% in most of the sensors. The cluster
 151 charge distributions are also reasonable. On the u/p-side, the most probable
 152 values agree with the calculated charge amount induced by MIPs within the
 153 uncertainty in calibration. On the v/n-side, 10–30% of the collected charge is
 154 lost compared to the signal collected on the u/p-side, due to the presence of the
 155 floating strip combined with the large pitch on the v/n-side. The most probable
 156 values of the cluster signal-to-noise ratio distributions range from 13 to 30.

157 We measured the cluster position resolution by analyzing the $e^+e^- \rightarrow \mu^+\mu^-$
 158 data [7]. The resolution is estimated from the residual between the cluster po-
 159 sition and the track position, not biased by the target cluster, after subtracting
 160 the effect of the track extrapolation error. The cluster position resolutions for
 161 different incident angles are shown in Fig. 3. The observed resolution has the
 162 expected shape, showing a minimum at the incident angle for which the projec-
 163 tion of the track along the direction perpendicular to the strips on the detector
 164 plane corresponds to two strip pitches. Given the various sensor pitches with
 165 one floating strip, the minimum is expected at 14 (21) degrees on the v/n-side
 166 and at 4 (7) degrees on the u/p-side, respectively for layer 3 (4, 5, and 6). The
 167 resolution for normal incident angle is also in good agreement with the expected
 168 digital resolution, that is 23 (35) μm on the v/n-side, 7 (11) μm on the u/p-side,
 169 respectively for layer 3 (4, 5, and 6). Still, some studies are ongoing to improve
 170 the resolution especially for the layer-3 u/p-side, where at normal incidence a
 171 slightly higher resolution is measured (9 μm) compared to the expectations.

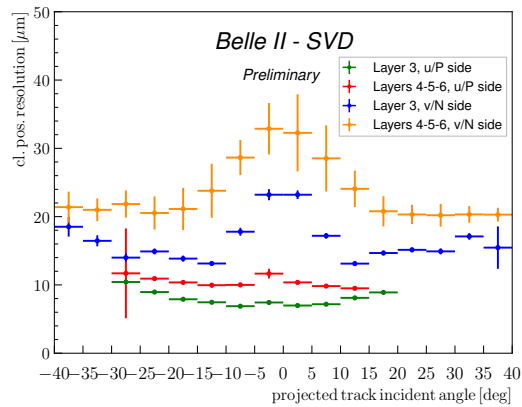


Figure 3: The SVD cluster position resolution depending on the projected track incident angle. The green (blue) plot shows the resolution in the u/p-side (n/v-side) of layer-3 sensors, and the red (yellow) one shows the u/p-side (n/v-side) of layers-4, 5, and 6 sensors.

172 The cluster hit-time resolution was also evaluated in candidate hadronic

173 events¹ using the reference event time estimated by the Central Drift Chamber
 174 (CDC) outside of the SVD. The error on the event time, about 0.7 ns, was
 175 subtracted to evaluate the intrinsic SVD hit-time resolution. The resulting
 176 resolution is 2.9 ns on the u/p-side and 2.4 ns on the v/n-side. With such
 177 precise hit-time information, it is possible to reject off-time background hits
 178 efficiently. The hit-time distributions for signal² and background³ are shown
 179 in Fig. 4. The signal distribution has a narrow peak, while the background
 180 hit-time distribution is broad and almost flat in the signal peak region. The
 181 separation power of the hit-time is high, as expected. For example, if we reject
 182 hits with the hit-time less than -38 ns in this plot, we can reject 45% of the
 183 background hits while keeping 99% of the signal hits. The background rejection
 184 based on the hit-time is essential to sustain the good tracking performance in
 185 the future high beam background condition.

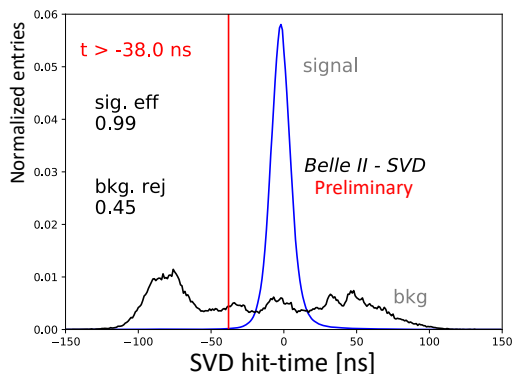


Figure 4: Example of the background hit rejection using hit-time. The blue distribution shows the signal, and the black distribution shows the background. The ordinates for signal and background are arbitrary normalized. Assuming the hit-time cut at -38 ns, the signal hit efficiency of 99% and the background hit rejection of 45% are achieved.

186 The performance in three-samples data was compared with that in six-

¹The events with more than three good tracks and not like Bhabha scattering.

²The clusters found to be used in the tracks in the hadronic events.

³The clusters in events triggered by delayed-Bhabha pseudo-random trigger.

187 samples data to evaluate the performance in the mixed-mode. If the trigger
 188 timing has no deviation, the three-samples data will show comparable perfor-
 189 mance to the six-samples data because the relevant part of the signal waveform
 190 to evaluate the necessary signal properties, i.e., the signal height and the sig-
 191 nal timing can be accommodated in the three-sample's time window. However,
 192 when the trigger has a jitter and the timing shift happens, some part of the
 193 signal waveform can be out of the three-sample's time window, and the recon-
 194 struction performance deteriorates. We examined the effect on the hit efficiency
 195 as a function of the trigger timing shift. The effect is evaluated by the rel-
 196 ative hit efficiency, which is defined as the ratio of the hit efficiency in the
 197 three-samples data to the one in the six-samples data. For this study, the three-
 198 samples data are emulated in the offline analysis from the six-samples data by
 199 selecting consecutive three samples at a fixed latency with respect to the Level-
 200 1 trigger signal. The trigger timing shift is evaluated by the CDC event time.
 201 The resulting relative efficiencies as a function of the trigger timing shift in the
 202 hadronic events are shown in Fig. 5. The decreasing trend is observed for the
 203 shift of the trigger timing, as expected. As a result, the relative efficiency is
 204 over 99.9% for the trigger timing shift within ± 30 ns, which is almost all the
 205 events.

206 **4. Beam-related background effects on SVD**

207 The beam-related background (BG) increases the hit occupancy of the SVD,
 208 which in turn degrades the tracking performance. Considering this performance
 209 degradation, we set the occupancy limit in layer-3 sensors to be about 3%, which
 210 will be loosened roughly by a factor of two after we apply the hit-time rejection
 211 described in Sec. 3. With the current luminosity, the average hit occupancy
 212 in layer-3 sensors is below 0.5%. However, the projection of the hit occupancy
 213 at the luminosity of $8 \times 10^{35} \text{ cm}^{-2}\text{s}^{-1}$ is about 3% in layer-3 sensors. The
 214 projected occupancy comes from the Monte Carlo (MC) simulation scaled by the
 215 data/MC ratio determined from the BG data of the current beam optics. The

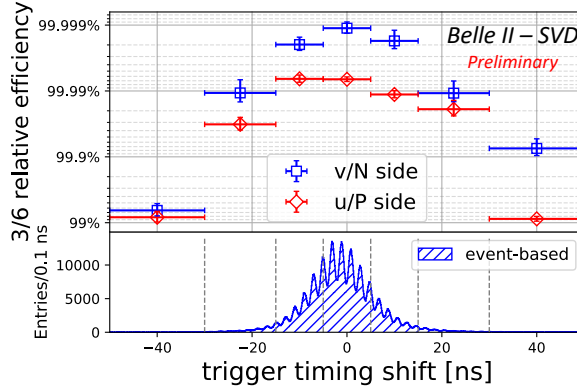


Figure 5: The relative hit efficiencies (the ratios of the hit efficiency in the three-samples data to the one in the six-samples data) as a function of the trigger timing shift for v/n-side (blue square) and u/p-side (red diamond). The positive (negative) trigger timing shift corresponds to early (late) trigger timing.

216 corresponding integrated dose, using the data/MC-rescaled BG extrapolation,
 217 is about 0.2 Mrad/smy, and the equivalent 1-MeV neutron fluence is about $5 \times$
 218 10^{11} $n_{\text{eq}}/\text{cm}^2/\text{smy}$ (smy: Snowmass Year = 10^7 sec). Considering the radiation
 219 hardness of the SVD sensors, about 10 Mrad and about 10^{13} $n_{\text{eq}}/\text{cm}^2$, based
 220 on the experience of similar DSSD sensors used in the BaBar Silicon Vertex
 221 Tracker [8], we expect to be able to safely operate the SVD even for ten years
 222 at high luminosity, with a safety margin of factor two to three against BG
 223 extrapolation. The long-term BG extrapolation is affected by large uncertainties
 224 from the optimization of collimator settings in MC and the future evolution
 225 of the beam injection background, which is not simulated. This uncertainty,
 226 together with the relatively small safety factor of two to three between the BG
 227 extrapolation and the detector limits, motivates the VXD upgrade to improve
 228 the tolerance of the hit rates and the radiation damage, and the technology
 229 assessment is ongoing for multiple sensor options.

230 In the first two and a half years of operation, the integrated dose in the
 231 layer-3 mid-plane sensors, which are the most exposed in the SVD, is esti-
 232 mated to be 70 krad. The estimation is based on the measured dose by the

233 diamonds on the beam pipe exploiting the measured correlation between the
234 SVD occupancy and the diamond dose [9]. Thanks to a new random trigger
235 line recently introduced, we improved the dose analysis, removing an overes-
236 timation of about factor three in the previous study. The new estimate still
237 has an uncertainty of about 50% mainly due to the unavailability of this newly
238 introduced trigger before December 2020. Assuming the dose/ n_{eq} fluence ra-
239 tio of 2.3×10^9 $n_{\text{eq}}/\text{cm}^2/\text{krad}$ from MC, 1-MeV equivalent neutron fluence is
240 evaluated to be about 1.6×10^{11} $n_{\text{eq}}/\text{cm}^2$.

241 Non-ionizing energy loss causes the lattice defects in the sensor bulk and
242 increases the sensor leakage current. The upper plot of Fig. 6 shows the linear
243 correlation between the current and the integrated dose. The slopes for all the
244 sensors are 2–5 $\mu\text{A}/\text{cm}^2/\text{Mrad}$, as summarized in the lower plot of Fig. 6. The
245 large variations can be explained by temperature effects and the deviation of
246 sensor-by-sensor dose from the average in each layer used in the estimation.
247 The slopes are in the same order of magnitude as previously measured in the
248 BaBar experiment [8], 1 $\mu\text{A}/\text{cm}^2/\text{Mrad}$ at 20°C. The precise temperature in
249 layer 3 of the SVD is unknown but expected to be in a similar regime. While
250 the leakage current is increasing, the impact on the strip noise is suppressed by
251 the short shaping time (50 ns) in APV25. It is expected to be comparable to
252 the strip-capacitive noise only after 10 Mrad irradiation and not problematic
253 for ten years where the integrated dose is estimated to be 2 Mrad.

254 The evolution of the noise with the integrated dose is shown in Fig. 7. The
255 noise increase of 20–25% is observed in layer 3, but this does not affect the
256 SVD performance. This noise increase is likely due to the radiation effects on
257 the sensor surface. Fixed oxide charges on sensor surface increase with dose,
258 with some saturation expected at around 100 krad, enlarging also non-linearly
259 the inter-strip capacitance, also expected to saturate with dose. The noise
260 saturation is already observed on the v/n-side and also starts to be seen on the
261 u/p-side.

262 The bulk damage also lowers the full depletion voltage of the sensor by
263 decreasing the carrier density of the n-type substrate. We measured the full

264 depletion voltage from the relation between the v/n-side strip noise and the
265 bias voltage. The result is consistent with measurements performed on the bare
266 sensors before the installation, ranging from 20 to 60 V, and so far no change in
267 full depletion voltage is observed in the first two and a half years of operation,
268 which is consistent with the expectation from low integrated neutron fluence of
269 $1.6 \times 10^{11} \text{ n}_{\text{eq}}/\text{cm}^2$.

270 **5. Conclusions**

271 The SVD has been taking data in Belle II since March 2019 smoothly and
272 reliably. The detector performance is excellent and agrees with expectations.
273 We are ready to cope with the increased background during higher luminosity
274 running by rejecting the off-time background hits using hit-time and operating
275 in the three/six-mixed acquisition mode. In the recent study, the efficiency
276 loss in the three-samples data is confirmed to be less than 0.1% for the trigger
277 timing shift within ± 30 ns. The observed first effects of radiation damage are
278 also within expectation and do not affect the detector performance.

279 **Acknowledgments**

280 This project has received funding from the European Union's Horizon 2020
281 research and innovation programme under the Marie Skłodowska-Curie grant
282 agreements No 644294 and 822070. This work is supported by MEXT, WPI,
283 and JSPS (Japan); ARC (Australia); BMBWF (Austria); MSMT (Czechia);
284 CNRS/IN2P3 (France); AIDA-2020 (Germany); DAE and DST (India); INFN
285 (Italy); NRF and RSRI (Korea); and MNiSW (Poland).

286 **References**

- 287 [1] T. Abe, et al., Belle II Technical Design Report (2010). arXiv:1011.0352.
288 [2] Y. Ohnishi, et al., Accelerator design at SuperKEKB, Prog. Theor. Exp.
289 Phys. 2013 (3), 03A011 (03 2013).

- 290 [3] S. Bacher, et al., Performance of the diamond-based beam-loss monitor sys-
291 tem of Belle II, Nucl. Instrum. Methods Phys. Res., Sect. A 997 (2021)
292 165157. arXiv:2102.04800.
- 293 [4] K. Adamczyk, et al., The Belle II silicon vertex detector assembly and me-
294 chanics, Nucl. Instrum. Methods Phys. Res., Sect. A 845 (2017) 38–42, pro-
295 ceedings of the Vienna Conference on Instrumentation 2016.
- 296 [5] M. J. French, et al., Design and results from the APV25, a deep sub-micron
297 CMOS front-end chip for the CMS tracker, Nucl. Instrum. Methods Phys.
298 Res., Sect. A 466 (2001) 359–365.
- 299 [6] G. Rizzo, et al., The Belle II Silicon Vertex Detector: Performance and
300 Operational Experience in the First Year of Data Taking, JPS Conf. Proc.
301 34 (2021) 010003.
- 302 [7] R. Leboucher, et al., Measurement of the cluster position resolution of the
303 Belle II Silicon Vertex Detector, these NIMA Conference Proceedings.
- 304 [8] B. Aubert, et al., The BaBar detector: Upgrades, operation and perfor-
305 mance, Nucl. Instrum. Methods Phys. Res., Sect. A 729 (2013) 615–701.
- 306 [9] L. Massaccesi, Performance study of the SVD detector of Belle II and future
307 upgrades, master thesis, Dipartimento di Fisica *E. Fermi*, Università di Pisa
308 (2021).
309 URL <https://docs.belle2.org/record/2759/>

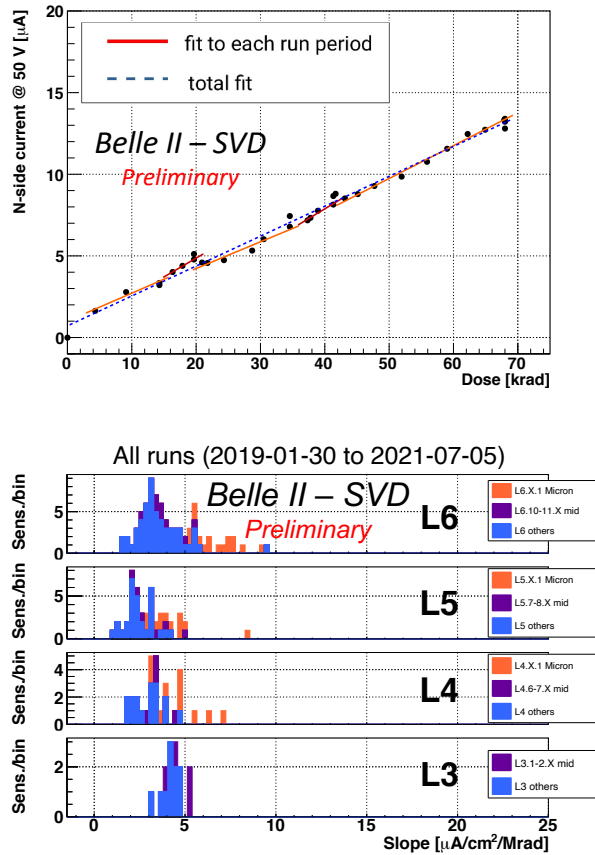


Figure 6: (upper) Effect of the integrated dose on the leakage current in the n/v-side of one layer-3 sensor. The slope is fitted for each run period (solid red line) and all the runs (dashed blue line). Both fit results agree with each other and are consistent with the linear increase. (lower) The fit results of all the sensors for all runs. The sensors are classified as trapezoidal sensors in the forward region (Micron), sensors around the midplane, and the others.

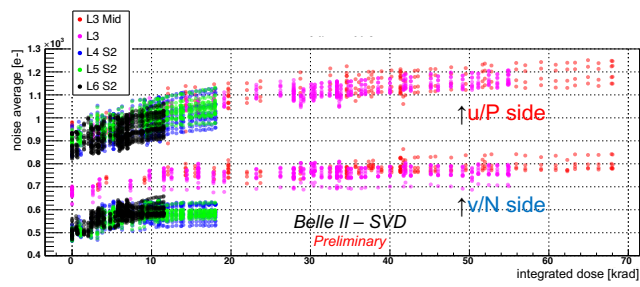


Figure 7: Effect of the integrated dose on the noise average in electron. The upper (lower) series shows the u/p-side (v/n-side) results, respectively.